

The Offset Filtration of Convex Objects*

Dan Halperin^{†1}, Michael Kerber^{‡2}, and Doron Shaharabani^{§1}

¹Tel Aviv University, Tel Aviv, Israel

²Max Planck Institute for Informatics, Saarbrücken, Germany

Abstract

We consider offsets of a union of convex objects. We aim for a filtration, a sequence of nested simplicial complexes, that captures the topological evolution of the offsets for increasing radii. We describe methods to compute a filtration based on the Voronoi partition with respect to the given convex objects. The size of the filtration and the time complexity for computing it are proportional to the size of the Voronoi diagram and its time complexity, respectively. Our approach is inspired by alpha-complexes for point sets, but requires more involved machinery and analysis primarily since Voronoi regions of general convex objects do not form a good cover. We show by experiments that our approach results in a similarly fast and topologically more stable method for computing a filtration compared to approximating the input by a point sample.

1 Introduction

Motivation The theory of *persistent homology* has led to a new way of understanding data through its topological properties, commonly referred as *topological data analysis*. The most common setup assumes that the data is given as a finite set of points and analyzes the sublevel sets of the distance function to the point set. An equivalent formulation is to take offsets of the point sets with increasing offset parameter and to study the changes in the hole structure of the shape obtained by the union of the offset balls; see Figure 1 for an illustration and informal description. Notice that we postpone the exposition of formal topology background to the next section.

We pose the question how to generalize the default framework for point sets to more general input shapes. While there is no theoretical obstacle to consider distance functions from shapes rather than points (at least for reasonably “nice” shapes), it raises computational questions: How can critical points of that distance functions be computed efficiently? And how can the topological information be encoded in a combinatorial structure of small size?

With the wealth of applications of barcodes of point sets, and together with the challenges raised by the extension from point sets to sets of convex objects, we believe that the latter is a logical next step of investigation. Our attention to this problem originates from the increasingly popular application of 3D printing. A common problem in this context is that often available models of shapes contain features that

*Work by D.H. and D.S. has been supported in part by the Israel Science Foundation (grant no. 1102/11), by the German-Israeli Foundation (grant no. 1150-82.6/2011), and by the Hermann Minkowski–Minerva Center for Geometry at Tel Aviv University. M.K. acknowledges support by the Max Planck Center of Visual Computing and Communication.

[†]danha@post.tau.ac.il

[‡]mkerber@mpi-inf.mpg.de

[§]doron.s@hotmail.com

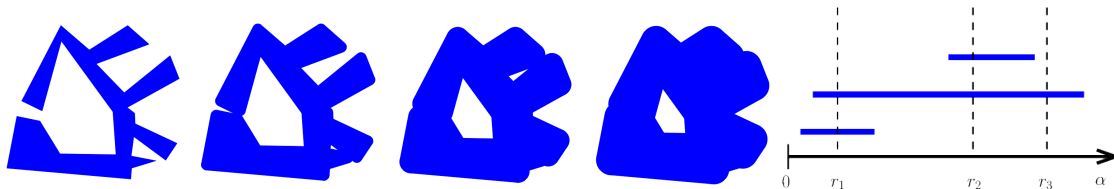


Figure 1: From left to right, we see an example shape, three offsets with increasing radii $r_1 < r_2 < r_3$, and the 1-barcode of the shape. While being simply-connected initially, two holes have been formed at radius r_1 , one of which disappears for a slightly larger offset value while the other one *persists* for a large range of scales. At r_2 , we see the formation of another rather short-lived hole. The barcode summarizes these facts by displaying one bar per hole. The bar spans over the range of offset radii for which the hole is present. We can read off the number of holes for radius α by counting the number of bars that have α in their x -range.

complicate the printing process, or turn it impossible altogether. A ubiquitous example is the presence of thin features which may easily break, and call for thickening. One work-around is to offset the model by a small value to stabilize it, but the optimal offset parameter is unclear, as it should get rid of many spurious features of the model without introducing too many new ones. Moreover, one would prefer *local thickening* [35], and possibly thickening by different offset size in different parts of the model. A by-product of our work here is a step toward automatically detecting target regions for local thickening that do not incur spurious artifacts. Persistent homology provides a *barcode* which constitutes a summary of the hole structure of the offset shape for any parameter value (Figure 1) which is clearly helpful for the choice of a good offset value. We are especially interested in an exact method in this context because any approximate barcode introduces artificial topological noise in addition to the real noise present in the model, which makes it even more difficult to choose a suitable offset radius.

Problem definition and contribution We design, analyze, implement, and experimentally evaluate algorithms for computing persistence barcodes of convex input objects. More precisely, we concentrate on the problem of computing a (*simplicial*) *filtration*, a sequence of nested simplicial complexes that undergoes the same topological changes as the offset shapes. Since the input objects are convex, the Nerve theorem asserts that the intersection patterns of the offsets (called the *nerve*) reveal the entire topological information. This leads to the generalization of Čech filtrations from point sets to our scenario. The resulting filtration has a size of $O(n^{d+1})$, where n is the number of input objects contained in d -dimensional Euclidean space. This size is already problematic for small d and a natural idea to reduce its size is to restrict the offset of each input object to its Voronoi regions, that is, the portion of the space which is closest to the object. This approach is again inspired by the analogue case of point sets, where *alpha-complexes* are preferred over the Čech complexes for small dimensions. However, the approach for point sets does *not* directly carry over to arbitrary convex objects: Voronoi regions of convex objects are not necessarily convex and can intersect in non-contractible patterns which prevents the application of the Nerve theorem.

We describe the construction of a filtration whose size is asymptotically equal to the complexity of the Voronoi diagram and yields the desired barcode. Conceptually, we subdivide the input objects into smaller sub-objects for which all intersections are empty or contractible and the Nerve theorem applies. Our algorithm computes the nerve of the sub-objects without performing the subdivision explicitly. We describe its details for \mathbb{R}^2 and sketch its generalization to convex polytopes in \mathbb{R}^3 . Our algorithm requires the computation of the Voronoi diagram of the input sites as a preprocessing step. We furthermore describe how the size of the output can be further reduced by an adaptive subdivision.

Finally, we show the surprising result that in \mathbb{R}^2 , the barcode of convex objects (without subdivision) is encoded in the barcode of their nerve, despite the presence of non-contractible intersections. The analogue statement in \mathbb{R}^3 is not true. While the proof ultimately still relies on the Nerve theorem, it requires a deeper

investigation of the structure of Voronoi diagrams of convex objects.

We have implemented our algorithm for polygons using the CGAL library and report on extensive experimental evaluation. In particular, we compare our approach with the natural alternative to replace the input polygons with sufficiently dense point samples. Although the point sample approach yields very close approximations to the exact barcode in a comparable running time, we demonstrate that the noise induced by the sampling results in additional noise on a large range of scales and therefore makes the topological analysis of the offset filtration more difficult.

Related work Since its introduction in [17], persistent homology has become an active area of research, including theoretical [7, 8, 12, 13], algorithmic [2, 10, 29, 39], and application [6, 11, 36] results (we only cite some representative references here). The information gathered by persistence is usually displayed either in terms of a barcode, e.g. [5], or via a *persistence diagram*, e.g. [12]. Both representations are equivalent and we adopt the barcode view in this work.

The textbook [16] describes the most common approaches for computing filtrations of point sets, including Čech- and alpha-complexes from above. Another common construction is the *Vietoris-Rips* complex which approximates the Čech complex in the sense that it is nested between two Čech complexes on similar scales; however, it is easy to see that this property does not carry over to the case of arbitrary convex objects.

Topological methods for shape analysis have been extensively studied: a commonly used concept are *Reeb graphs* which yield a skeleton representing the connectivity of the shape and can be seen as a special case of persistent homology in dimension 0; see [4] for ample applications. The full theory of persistent homology has also been applied to various tasks in shape analysis, including shape segmentation [34] and partial shape similarity [18]. While these works study the *intrinsic* properties of a shape through descriptor functions independent of the embedding, our problem setup rather asks about *extrinsic* properties, that is, how the shape is embedded in ambient space.

Voronoi diagrams are one of the most basic objects in computational geometry [1, 14, 19]. Efficient algorithms for the case of point sets have been designed and implemented in 2D and 3D [31, 33, 38] and higher dimensions [23]. In the plane, generalizations to convex objects [25] and line segments and circular arcs [21] have been presented. Generalizations in three dimensions include Voronoi diagrams of (infinite) lines [22] and approximating the Voronoi diagram of one polyhedron [28]. However, no exact and efficient method is available for a set of (convex) polyhedra in \mathbb{R}^3 ; we refer to [37] for a discussion of the difficulties.

Outline We describe the direct approach to compute barcodes of convex objects, generalizing Čech complexes, in Section 2, introducing the required topological concepts. We describe our more efficient filtration based on Voronoi diagrams in Section 3 and report on experimental evaluations in Section 4.

2 Topological background

We review standard notation and basic results in persistent homology and dualizations of set covers through nerves. This assumes some familiarity with basic topological notions, in particular simplicial complexes and homology groups; the necessary background is covered by the textbook [16] and in more detail by [20, 30].

Persistent homology A *filtration* is a collection of spaces $(Q_\alpha)_{\alpha \geq 0}$ with the property that $Q_{\alpha_1} \subseteq Q_{\alpha_2}$ whenever $\alpha_1 \leq \alpha_2$. We say that α is a *homologically critical value* if $H_p(Q_{\alpha-\varepsilon})$ is not isomorphic to $H_p(Q_\alpha)$ for some $p \geq 0$ and any $\varepsilon > 0$ small enough, with $H_p(Q_\alpha)$ being the p -th (singular) homology group of Q_α with respect to an arbitrary fixed base field. We assume the usual *tameness conditions* that the homology groups of each Q_α have finite rank, and the number of homologically critical values is finite. The inclusion map from Q_{α_1} to Q_{α_2} induces a map $F_{\alpha_1, \alpha_2} : H_p(Q_{\alpha_1}) \rightarrow H_p(Q_{\alpha_2})$ for any p . The collection of

homology groups $(H_p(Q_\alpha))_{\alpha \geq 0}$ together with the morphisms F_\cdot , are an example of a *persistence module*. An homology class $[c] \in H_p(Q_\alpha)$ is *born at α* , if $[c] \notin \text{im} F_{\alpha-\varepsilon, \alpha}$ for any $\varepsilon > 0$. A class $[c]$ born at α *dies at β* , if $[c] \in \text{im} F_{\alpha-\varepsilon, \beta}$, but $[c] \notin \text{im} F_{\alpha-\varepsilon, \beta-\varepsilon}$. In this way, every homology class in $H_p(Q_\alpha)$ for any α is assigned to a birth-death interval; the *p-th barcode* of the filtration $(Q_\alpha)_{\alpha \geq 0}$ is the set of these intervals. The length of the birth-death interval is called the *persistence* of the corresponding homology class. Usually, persistence is interpreted as a measure of importance for a class, since persistent classes represent the homological features of the given space that are present on many different scales.

An important notion in this context is the distance between persistence modules which allows to define approximations of barcodes. While such distances can be defined for arbitrary persistence modules [7], we need only a simplified setup in our work: For $\varepsilon > 0$, we call two filtrations $(F_\alpha)_{\alpha \geq 0}$ and $(G_\alpha)_{\alpha \geq 0}$ *ε -interleaved*, if for any $\alpha > 0$, it holds that $F_\alpha \subseteq G_\alpha \subseteq F_{\alpha+\varepsilon}$. Informally speaking, the bars of two ε -interleaved filtrations are in one-to-one-correspondence to each other, and the birth- and death-values of corresponding bars differ by at most ε .

Nerves Let $\mathcal{P} := \{P^1, \dots, P^n\}$ be a collection of non-empty sets in a common domain. The *underlying space* is defined as $|\mathcal{P}| := \bigcup_{i=1, \dots, n} P^i$. We call a non-empty subset $\{P^{i_1}, \dots, P^{i_k}\} \subseteq \mathcal{P}$ *intersecting*, if $\bigcap_{j=1}^k P^{i_j} \neq \emptyset$. The *nerve* $\mathcal{N}(\mathcal{P})$ of \mathcal{P} is the collection of all intersecting subsets. It is clear by definition that every singleton set $\{P^i\}$ is in the nerve, and that any non-empty subset of an intersecting set is also intersecting. The latter property implies that the nerve is a *simplicial complex*: the singleton sets $\{P_i\}$ are the *vertices* of that complex. Since simplicial complexes are topological spaces, the homology groups of $\mathcal{N}(\mathcal{P})$ are well-defined. We call \mathcal{P} a *good partition* if all sets in the collection are closed and triangulable, and any intersecting subset yields a contractible intersection.

Theorem 1 (Nerve Theorem). *If \mathcal{P} is a good partition, $|\mathcal{P}|$ is homotopically equivalent to $\mathcal{N}(\mathcal{P})$. In particular, $H_p(|\mathcal{P}|) = H_p(\mathcal{N}(\mathcal{P}))$ for all $p \geq 0$.*

A case of special importance for us is that all P^i are closed convex sets, in which the Nerve Theorem applies, because convex sets are contractible and the intersection of convex sets is convex. Of paramount importance for our work will be that the isomorphism between the homology groups of $|\mathcal{P}|$ and $\mathcal{N}(\mathcal{P})$ commutes with inclusions. This is asserted by the following lemma which is a slightly modified version of [9, Lemma 3.4].

Theorem 2 (Chazal and Oudot). *Let $\mathcal{P} := \{P^1, \dots, P^n\}$ and $\mathcal{Q} := \{Q^1, \dots, Q^n\}$ be good partitions with $P^i \subseteq Q^i$ for all $i = 1, \dots, n$. Then, the isomorphisms $\phi_{\mathcal{P}} : H_p(|\mathcal{P}|) \rightarrow H_p(\mathcal{N}(\mathcal{P}))$ and $\phi_{\mathcal{Q}} : H_p(|\mathcal{Q}|) \rightarrow H_p(\mathcal{N}(\mathcal{Q}))$ commute with the maps $i^* : H_p(|\mathcal{P}|) \rightarrow H_p(|\mathcal{Q}|)$ and $j^* : H_p(\mathcal{N}(\mathcal{P})) \rightarrow H_p(\mathcal{N}(\mathcal{Q}))$ that are induced by canonical inclusions, that is, $j^* \circ \phi_{\mathcal{P}} = \phi_{\mathcal{Q}} \circ i^*$.*

Barcodes of shapes Let P^1, \dots, P^n be convex polyhedra in \mathbb{R}^d , that is, each P^i is the intersection of finitely many halfspaces, and let $P := P^1 \cup \dots \cup P^n \subset \mathbb{R}^d$ denote their union. We let $d(\cdot, \cdot)$ denote a distance function; for simplicity, we consider the case of the Euclidean distance while noting that our results extend to arbitrary strictly convex distance functions. For a point set $A \subset \mathbb{R}^d$ and $x \in \mathbb{R}^d$, we set $d(x, A) := \min_{y \in A} d(x, y)$. Then, $d(\cdot, A) : \mathbb{R}^d \rightarrow \mathbb{R}$ is called the *distance function from A* and $A_\alpha := \{x \in \mathbb{R}^d \mid d(x, A) \leq \alpha\}$ is called the *α -offset* of A. As a notational shortcut, we will write $d(x) := d(x, P)$ when P is obvious from the context. We call $(P_\alpha)_{\alpha \geq 0}$ the *offset-filtration* of P. We pose the question of how to compute the barcode of this offset filtration. See Figure 1 for an illustration of these concepts.

We define the analogue of Čech filtrations for unions of convex shapes: The decomposition of P into subpolygons induces a filtration of nerves. To define it, we let $\mathcal{P}_\alpha := \{P_\alpha^1, \dots, P_\alpha^n\}$, where P_α^k is the α -offset of P_k . We write \mathcal{P} for \mathcal{P}_0 for notational convenience. We call $(\mathcal{N}(\mathcal{P}_\alpha))_{\alpha \geq 0}$ the *nerve filtration* of P (with respect to P^1, \dots, P^k); it is indeed a filtration because for $\alpha_1 \leq \alpha_2$, $\mathcal{N}(\mathcal{P}_{\alpha_1}) \subseteq \mathcal{N}(\mathcal{P}_{\alpha_2})$.

Theorem 3. *The p -th barcode of the offset filtration and of the nerve filtration are equal for any $p \geq 0$.*

Proof. The Nerve theorem yields an isomorphism of the homology groups for any parameter α and Theorem 2 asserts that these isomorphisms commute with inclusion. Using the *persistence equivalence theorem* [16, p.159], the barcodes are equal. \square

The nerve only changes for values where a collection of individual polyhedron offsets becomes intersecting. We call such an offset value *nerve-critical*. Since $P \subset \mathbb{R}^d$, we can restrict to collections of size at most $d + 1$ since the p -th barcode is known to be trivial for $p \geq d$. Sorting the nerve-critical values $0 = \alpha_0 < \alpha_1 < \dots < \alpha_m$ and setting $K_i := \mathcal{N}(\mathcal{P}_{\alpha_i})$, the nerve filtration simplifies to the finite filtration

$$K_0 \subset K_1 \subset \dots \subset K_m, \tag{1}$$

whose barcode can be computed using standard methods; see [17, 39] or [2] for an optimized variant. Clearly, since K_m contains a simplex for any subset of \mathcal{P} of size at most $d + 1$, its size is $\Theta(n^{d+1})$.

To complete the algorithmic description, we need to specify how to compute the nerve-critical values. We assume that the ambient dimension d is a constant. If each input polygon has a constant number of boundary vertices, the nerve-critical values can be computed in constant time using a brute force approach, by solving several quadratic inequalities. More effort is needed, however, if the input polygons can be arbitrarily complex. Were we dealing with polygonal metrics, the problem could be rephrased as a simple linear program whose constraints can be derived from a Minkowski sum computation. The Euclidean (L_2) case can either be solved by a polygonal metric that approximates the unit disk, or by an LP-type [27] approach. Since in the sequel, we assume that the input objects have complexity bounded by a constant, we defer further discussion of the more general case to the full version of the paper.

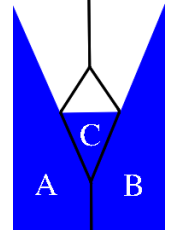
3 Restricted barcodes

The major disadvantage of the construction of Section 2 is the sheer size of the resulting filtration, $\Theta(n^{d+1})$, for n convex objects in \mathbb{R}^d . Our goal is to come up with a filtration that yields the same barcode and is substantially smaller in size. Our approach, which we describe next, is reminiscent of alpha-complexes for point sets, but it requires additional ideas for being applicable to convex objects.

Restricted nerve filtrations We assume for simplicity that the elements of $\mathcal{P} = \{P^1, \dots, P^n\}$ are pairwise interior-disjoint convex polyhedra. We refer to them as *sites* from now. For a point $p \in \mathbb{R}^d$, the site P^k is *closest* if $d(p, P^k) \leq d(p, P^\ell)$ for any $1 \leq \ell \leq n$. We assume general position, which means that no point has more than $d + 1$ closest sites. The *Voronoi diagram* is the partition of the space into maximal connected components with the same set of closest sites. The Voronoi diagram is a cell complex in \mathbb{R}^d , and its *combinatorial complexity* is the number of cells. The *Voronoi region* of P^k , denoted by V^k , is the set of points for which P^k is one of its closest sites.

The *restricted α -offset* of P^k is defined as $Q_\alpha^k := P_\alpha^k \cap V^k$. We set $\mathcal{Q}_\alpha := \{Q_\alpha^1, \dots, Q_\alpha^n\}$ and $\mathcal{Q} := \mathcal{Q}_0$. In the same way as in Section 2, we define the *restricted nerve filtration* as $(\mathcal{N}(\mathcal{Q}_\alpha))_{\alpha \geq 0}$ and \mathcal{Q} -critical values as those values where a simplex enters the restricted nerve filtration. The restricted nerve filtration can be expressed by a finite sequence of simplicial complexes as in (1) that changes precisely at the \mathcal{Q} -critical values. The simplices of that filtration are in one-to-one correspondence with the cells of the Voronoi diagram, therefore the size of the filtration equals the combinatorial complexity of the Voronoi diagram. Moreover, the \mathcal{Q} -critical value of a simplex associated with a Voronoi cell C is equal to $\min_{x \in C} d(x)$ (recall that $d(x) = d(x, P)$). A point x for which the minimum is attained is called a *critical point* of that cell. Critical points might not be unique for a cell, but they form a connected subset, as will be shown later on. Note that all critical points of a cell may lie on its boundary.

Restricting the offsets to Voronoi regions brings a problem: \mathcal{Q}_α is not necessarily a collection of convex sets, since V^k is not convex in general. For instance, in the situation depicted on the right, we see three sites A, B, C and the induced Voronoi diagram (in black). We see that the Voronoi regions of A and B intersect in two segments. This means that the proof of Theorem 3 breaks down since the restricted offsets do not form a good partition, and therefore are not guaranteed to give the same barcode as the offset filtration.



Subdivision From now on, we focus on the case $d = 2$, that is, the sites are interior-disjoint polygons in the plane. For simplicity of analysis, we also assume that the number of edges (and vertices) on the boundary of each convex site is bounded by a small constant. We leave the more detailed analysis for future work. Reconsidering the counterexample from above, the reason for the non-contractible intersections was a small site sitting in between two lengthy sites. A natural idea is to split the lengthy sites into smaller sub-sites in a way that every piece of the original bisector is associated with a distinct pair of sub-sites. In the example above, it would suffice to cut A and B along a common horizontal line that goes through the interior of C . It should not be surprising that a sufficiently fine splitting will always avoid non-contractible intersection, but the question remains how many splits are necessary. We show that a total number of ν sub-sites suffices, where ν is the combinatorial complexity of the Voronoi diagram. Afterwards, we will see that the nerve filtration induced by the sub-sites can be computed entirely from the combinatorial data provided by the Voronoi diagram of the original sites, which means that the subdivision does not have to be performed explicitly for the computation.

Fix a site S and let V denote its Voronoi region. We will not subdivide S directly, but rather subdivide its ε -offsets S_ε , where ε is an arbitrarily small value. We refer to S_ε as ε -site, and define the map $\pi : \partial V \rightarrow \partial S_\varepsilon$, which assigns to each $v \in \partial V$ its closest point on S_ε . We note that ε only exists conceptually, and the value never needs to be specified in the algorithm.

Lemma 4. *The map π is well-defined and injective.*

Proof. We shall first show that π is well-defined, that is, every $p \in \partial V$ is closest to a single point $q \in \partial S_\varepsilon$. Assume by contradiction that it is not, so there are $q_1, q_2 \in \partial S_\varepsilon$ such that $d(p, q_1) = d(p, q_2)$ and that distance is minimal over all points in ∂S_ε . Then a disk of radius $d(p, q_1)$ centered at p touches S_ε at q_1 and q_2 and intersects no other points of S_ε in its interior. This however implies that S_ε is not convex, due to the disk being strictly convex, which leads to a contradiction.

Assume by contradiction that π is not injective. So there are $p_1, p_2 \in \partial V$ such that $p_1 \neq p_2$ and $\pi(p_1) = \pi(p_2) = q$. As described above, there exist two disks, one centered at p_1 and one centered at p_2 , that touch S_ε at q . The tangents to the two disks at q are also tangent to S_ε at q . However due to ε -offsetting, S_ε has one unique tangent at any point. This implies that the two disks are the same, thus contradicting $p_1 \neq p_2$. \square

The injectivity of π is of high importance to showing the correctness of our method, and is the main reason for subdividing S_ε instead of S . Injectivity is lost if π maps to ∂S instead of ∂S_ε .

Next, we are going to split the ε -sites. The *bisector* of two sites is the set of points which have the same distance to both sites. The boundary of any Voronoi region consists of a set of *bisector segments*, each being a connected subset of a bisector of two sites. For each bisector segment, choose an arbitrary point in its interior, called its *anchor*. For each Voronoi region, choose a point in the interior of its site, called the *center* of the Voronoi region. For a bisector segment with anchor a bounding the Voronoi cell V of an ε -site S_ε , we let $\pi(a)$ denote its *inner anchor* on S_ε . Because of injectivity, no two inner anchors coincide. We connect each inner anchor on S to the center of S by a straight line segment. Clearly, these segments split the ε -site into sub-sites which we refer to as *refined sites*. See Figure 2 for an illustration of a subdivision, and an illustration of the problems of the construction when directly performed on an original input site S without

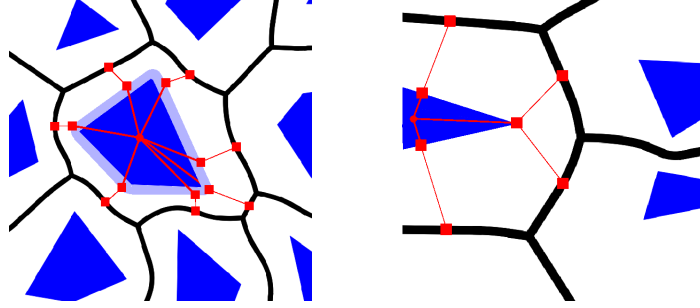


Figure 2: Left: Example of the subdivision. The shaded area denotes the ε -offset of the site drawn in dark. The inner anchors are drawn on the boundary and are connected to the center by thick (red) line segments and to the anchor by a bisector drawn as thin (red) segment. Right: If the inner anchors would have been taken on the boundary of the site directly (without the ε -offset), two inner anchors would coincide, and the construction would not yield a partition into Voronoi regions.

ε -offset. We define a *refined Voronoi region* to be the Voronoi region of a refined site. The refined Voronoi regions form a good partition, as shown in the next lemma.

Lemma 5. *The refined Voronoi regions form a good partition.*

Proof. Any such region is contractible, accounting for subsets of size one. We show that the intersection of a pair (W^1, W^2) of refined Voronoi regions is contractible: If two refined regions belong to the same original region, their intersection is either only the center or one or two paths from the center to an anchor and thus contractible. If the refined regions come from different original regions, say W^1 from V^1 and W^2 from V^2 , their intersection is a subset of $V^1 \cap V^2$. Assume that it is non-contractible. Then, the intersection contains at least one point of two distinct bisector segments that are both subsets of the bisector of V^1 and V^2 . That implies that W^1 contains a path on the boundary of V^1 connecting these two bisector segments. This means that it contains a complete bisector segment between them, which is a contradiction because we have placed a single anchor on any bisector segment.

The case of three and more intersecting pieces follows from the cases of pairs. We refer to Appendix A for details. \square

From Lemma 5 it follows that for a large enough α , such that any α -offset of a refined site fills its refined Voronoi region, the restricted α -offsets of the refined sites form a good partition. We would like to prove that the property holds for any α . Intersections between restricted offsets of refined sites can only occur on the boundary of their Voronoi regions, along a shared bisector segment. The following Lemma examines the intersection of an offset of a refined site and a bisector.

Lemma 6. *Let B be the bisector of the two sites R^1 and R^2 , and let $\rho : B \rightarrow \mathbb{R}$ be a function that assigns to a point $x \in B$ the value $d(x, R^1)$. Then the sublevel sets of ρ form a connected subset.*

Proof. Fix $\alpha > 0$ and consider the sublevel set $\rho^{-1}(-\infty, \alpha)$ on B . Assume for a contradiction that it consists of two components. Since ρ is continuous and goes to ∞ when we follow the bisector to either side, disconnectedness of the sublevel set implies that there are at least 4 points on B with ρ -value α . These four points lie on the intersections of the Minkowski sums $R^1 \oplus B_\alpha$ and $R^2 \oplus B_\alpha$, where B_α is the disk of radius α centered at the origin. This, however, contradicts the *pseudo-disk property* of Minkowski sums of convex sets [26] which states that the boundaries can only intersect twice. \square

We can now prove that the restricted offsets of the refined sites form a good partition.

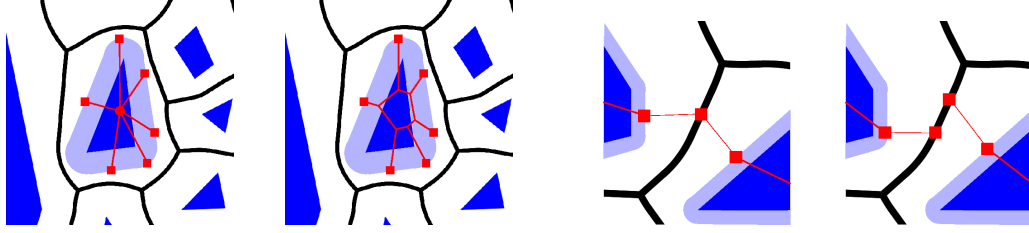


Figure 3: Removing degeneracies. From left to right: Several refined sites of a single input site meet at the center (1st). We resolve this by replacing the center point with a center site of small diameter. (2nd). At anchors, the Voronoi regions of four refined sites meet (3rd). We can replace the anchor by a pair of anchors for opposite regions (with small distance between the anchors) to resolve the degeneracy (4th).

Lemma 7. *For any $\alpha \geq 0$, the restricted α -offsets of refined sites form a good partition.*

Proof. For $\alpha < \infty$, we consider only the intersection of two restricted offsets; the case of higher-order intersections follows again from the results of Appendix A. Assume that R^1 and R^2 are refined sites whose restricted alpha-offsets intersect. The intersection is a subset of the intersection I of their Voronoi regions and I is connected, as we have proved in Lemma 5. Let B be the bisector of R^1 and R^2 . The function $\rho : B \rightarrow \mathbb{R}$ as defined above has the property that any sublevel set is connected (Lemma 6). The intersection of the restricted α -offsets of R^1 and R^2 , however, is equal to $I \cap \rho^{-1}[0, \alpha]$, and therefore homeomorphic to the intersection of two intervals. \square

The union of α -offsets of the restricted sites equals the union of $(\alpha + \varepsilon)$ -offsets of the original sites. Therefore, the barcodes are the same up to an ε -shift. Moreover, for each offset value, we have a good partition which implies that the restricted nerve filtration of the refined sites yields the same barcode. It is important to remark that this property holds for any choice of anchor points. Also, note that our construction yields a degenerate setup as more than 3 Voronoi regions meet at a point. However, resolving these cases is an easy task – we refer to Figure 3 for further explanations.

Computing the nerve We explain now how to compute the nerve of the refined sites just constructed. We assume that our input consists of a planar subdivision (represented as a doubly-connected edge list, or DCEL for short [14, Ch.2]) which represents the Voronoi diagram and consists of vertices, edges, and faces. The edges represent the bisector segments, which may be composed of several different curves, the faces represent Voronoi regions. The vertices represent points where bisector segments intersect. By our general position assumption, every finite vertex is incident to exactly three faces. For simplicity, we assume that unbounded edges have distinct infinite endpoints which are incident to two faces. Every vertex, edge and face can access incident features efficiently. We assume that every (finite) vertex and every edge also has stored its critical value, that is, the critical value for the collection of sites that are incident to it. The output is a filtration, that is, a sequence of simplices sorted by filtration values such that every prefix is a simplicial complex. We incorporate the handling of degeneracies as described in Figure 3 — this is essential in order to guarantee a small size of the resulting filtration. We shall now describe the algorithm.

For every vertex v_i of the Voronoi diagram of the input sites, and each face f_x that is incident to it, we create a nerve vertex $\bar{v}_{i,x}$ representing a refined site. In particular, we create three nerve vertices per finite and two nerve vertices per infinite vertex. For each face f_x , we create an additional nerve vertex \bar{v}_x , representing the refined site around the center as in Figure 3. For each nerve vertex $\bar{v}_{i,x}$ we add the nerve edge $\bar{v}_{i,x}\bar{v}_x$. We traverse the boundary of each face f_x . For every two neighboring vertices v_i, v_j on the boundary we add the nerve edge $\bar{v}_{i,x}\bar{v}_{j,x}$ and the nerve triangle $\bar{v}_{i,x}\bar{v}_{j,x}\bar{v}_x$. All simplices created so far get filtration value 0.

Next we iterate over all edges of the Voronoi diagram. For an edge e with critical value w incident to vertices v_1 and v_2 and faces f_x and f_y , we fetch the four nerve vertices representing the incident refined sites:

$\bar{v}_{1,x}$, $\bar{v}_{1,y}$, $\bar{v}_{2,x}$, and $\bar{v}_{2,y}$. Note that the edges $\bar{v}_{1,x}\bar{v}_{2,x}$ and $\bar{v}_{1,y}\bar{v}_{2,y}$ were already created in the previous step. We create the nerve edges $\bar{v}_{1,x}\bar{v}_{1,y}$, $\bar{v}_{2,x}\bar{v}_{2,y}$, and $\bar{v}_{1,x}\bar{v}_{2,y}$, and the nerve triangles $\bar{v}_{1,x}\bar{v}_{1,y}\bar{v}_{2,y}$ and $\bar{v}_{1,x}\bar{v}_{2,x}\bar{v}_{2,y}$ (the nerve edge $\bar{v}_{2,x}\bar{v}_{1,y}$ and its two incident nerve triangles are not added to resolve degeneracies as on the right of Figure 3). They all get w as their filtration value.

Finally, we iterate over the finite vertices of the diagram. For each vertex v_i with critical value w , let $\bar{v}_{i,x}$, $\bar{v}_{i,y}$, $\bar{v}_{i,z}$ denote the associated nerve vertices. All nerve edges between them were created in the previous step. We create the nerve triangle $\bar{v}_{i,x}\bar{v}_{i,y}\bar{v}_{i,z}$ with filtration value w . That ends the description of the algorithm.

The Voronoi diagram of the polygons is a subset of the Voronoi diagram of the line segments bounding the polygons, and therefore it can be computed in time $O(n \log n)$ and is of size $O(n)$. We perform a constant number of operations per face, edge and vertex of the diagram leading to a total running time of $O(n \log n)$. The following theorem shows that the outcome is correct.

Theorem 8. *The barcode of the filtration computed by the algorithm above equals the barcode of the offset filtration of the original sites.*

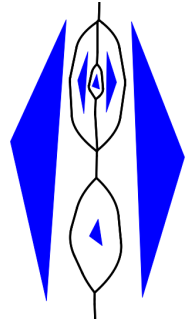
Proof. We first show that the algorithm computes a filtration that is ε -interleaved with the nerve filtration of the refined sites: As noted, the barcode for the refined sites is independent of the chosen anchor points. Assume that we place every anchor sufficiently close to the critical point of the segment. Then, the refined sites around that anchor become intersecting for a radius between w and $w + \varepsilon$ where w is the critical value of the segment. Our algorithm assigns value w to them, thus changing the filtration value by at most ε . This is sufficient to prove that the filtrations are ε -interleaved.

To finish the proof, note that the offset filtration equals the offset filtration of the refined sites up to an ε -shift, so both filtrations are ε -interleaved. The barcodes of the offset and nerve filtration of refined sites are equal by Lemma 7. The latter is ε -interleaved with the filtration formed by the algorithm. It follows that the two barcodes in question are 2ε -interleaved, that is, the bars are in one-to-one correspondence such that corresponding bars have the same length up to a function in ε . However, neither barcode depends on ε , and ε can be chosen arbitrarily small, so the barcodes must be the same. \square

Size and optimizations For an input of n sites, let C_n denote the maximal complexity of the Voronoi diagram, that is, its total number of sites, bisector segments, and Voronoi vertices. The algorithm described above creates one refined site per face of the diagram, representing its center site, and 3 refined sites per vertex of the diagram, thus creating at most $3C_n$ refined sites. The restricted nerve that we construct creates exactly one simplex per feature of the Voronoi diagram of the refined sites. Its complexity is therefore C_{3C_n} . Since $C_n \leq c \cdot n$ for some constant c , the complexity of the nerve is bounded by $3c^2n$ and thus stays linear.

We can lower the constant with small effort. Note that it is sufficient to place an anchor only between two bisector segments that come from the same bisector. Such anchors can be identified by a simple greedy traversal of the boundary of a Voronoi region. The proof of Lemma 5 carries over and ensures the correctness of the barcode. Also, the combinatorial nerve construction algorithm can be easily adapted to this sparse subdivision.

In order to bound the number of anchors required for the sparse subdivision, we analyze in more detail what causes two sites to have a non-contractible intersection. Note that a non-contractible intersection only happens when a bisector between two sites contributes two or more bisector segments to the Voronoi diagram. In short, this only happens if the bisector is *split* by another site that “sits between” the sites that define the bisector. Precisely, we observe that the intersection of two sites V^i , V^j consists of k connected components (with $k \geq 1$) if and only if the complement of $V^i \cup V^j$ induces $k - 1$ bounded regions. We call these bounded regions *surrounded region* induced by V^i and V^j . A surrounded region is again the union of one or more Voronoi regions and can therefore



contain nested surrounded regions (induced by two Voronoi regions within the surrounded regions). On the right, we see an example where the left and right sites induced two surrounded regions, the upper one containing a nested surrounded region. By showing that there cannot be more than n surrounded regions in total, we get the following bound.

Lemma 9. *The sparse subdivision yields a collection of at most $4n$ refined sites. In particular, its nerve filtration is of size C_{4n} .*

Proof. We first bound the number of surrounded regions by n : if a surrounded region has no nested surrounded region, we charge it to some Voronoi region that is contained in it. If it does have a nested surrounded region, we charge it to one of the Voronoi regions that induces a nested surrounded region. In this way, every Voronoi region is charged at most once, which implies the bound.

In view of the definition of surrounded regions, the sparse subdivision cuts a polygon in two parts whenever it detects a surrounded region. Since a surrounded region is induced by 2 Voronoi regions and there are at most n surrounded regions, there are at most $2n$ splits in total, resulting in $3n$ refined sites. Additionally, we have to place refined sites in the center of each original site to ensure generic position, increasing the size by at most n . \square

We can go further: By investigating the structure of surrounded regions more carefully, we can prove that subdividing the sites is not necessary!

Theorem 10. *For convex polygonal sites in \mathbb{R}^2 , the 0- and 1-barcode of the restricted nerve filtration are equal to the 0- and 1-barcode of the offset filtration, respectively.*

In light of this result, one may wonder why we consider the subdivision approach at all. One reason is that the equivalence of Theorem 10 does not extend to higher dimensions. For instance, in the situation depicted on the right, we see four sites in \mathbb{R}^2 where every triple of Voronoi regions intersects, but there is no common intersection of all four of them. Consequently, their nerve consists of the four boundary triangles of a tetrahedron and therefore carries non-trivial 2-homology. We refer to such homology classes as “ghost features”. In the planar case, the offset filtration can clearly not form any void (a 3-dimensional hole) and we can therefore safely ignore all ghosts. In \mathbb{R}^3 , however, the 2-barcode carries information about the offset and the ghosts need to be distinguished from real features. If ghost features had infinite persistence, we could simply filter them out, because any real 2-homology class dies eventually, just because the enclosed void is filled eventually. We can quite easily, however, construct an example of a ghost with finite lifetime: We create 4 triangular prisms with vertical axis in z -direction. All prisms start at level $z = 0$, and their bottom triangles form a situation like in Figure 4, that is, they create a ghost. We let the two outer prisms extend up to $z = 1$, and the two inner prisms to extend to $1 - \varepsilon$. Considering the Voronoi diagram, we can observe that their four Voronoi regions have a common intersection at a very high z -level. That means, for a sufficiently large offset value, the tetrahedron will be filled and the ghost feature dies.

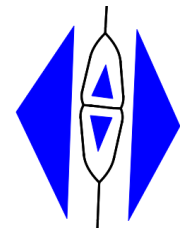


Figure 4: A ghost sphere

Another reason for considering the subdivision approach is that the refined nerve filtration obtained using it allows the computation of the barcode in near-linear time using a combination of Alexander duality and union-find as in [15]. This seems unclear for the unsubdivided filtration because the additional 2-homology prevents a direct application of Alexander duality. Therefore, one has to fall back to the general (and slower) persistence algorithm which balances out the advantage of a smaller filtration size partially.

The proof of Theorem 10 requires substantially more algebraic machinery than what we have introduced; we refer to Appendix A for details and only sketch the main ideas for brevity. A non-contractible intersection of two restricted offsets of sites A and B is caused by a surrounded region containing one or more other interior sites. The crucial observation is that the (unrestricted) offsets of A and B (with same radius) fill

the entire surrounded region. This implies that we can mark all interior sites as *inactive*, meaning that we remove them from consideration when the offset radius exceeds a certain threshold without changing the union of the offsets. For any α , the restricted offsets of active sites form a good partition, and their union covers the same space as the union of all sites, asserting that the homology of the nerve of restricted active offsets equals the homology of the offsets of the input sites for all $\alpha \geq 0$.

The first major result we show is that the nerve of restricted active offsets has the same 0- and 1-homology as the nerve of all restricted offsets. The statement is incorrect for 2-homology (Figure 4 is a counterexample). The proof (for 1-homology) is based on an explicit construction that transforms any 1-cycle in the nerve of all sites to an homologous cycle that only includes active sites. This results show that for each α , the 0- and 1-homology of the α -offsets of the input sites and their (restricted) nerves are equal.

To finish the proof, we have to show that the induced isomorphisms commute with inclusions. This case is not covered by Theorem 2 because the offsets do not form a good partition. Instead, we consider the nerve “filtration” of restricted active sites as an intermediate structure. It is not a filtration in the sense of this paper because sites disappear from the nerve when becoming inactive, so the simplicial complexes are not nested. Still, the nerves can be connected by *simplicial maps* instead of inclusions and the concept of barcodes extends to this setup. As second major result, we show that the isomorphism induced by the Nerve theorem between offsets sites and nerve of restricted active offsets commutes with these simplicial maps. The proof requires the study of this isomorphism in detail and extends the proof of Theorem 2 in this generalized setting.

Restricted barcodes in 3D While Theorem 10 does not generalize for higher-dimensional shapes, the ideas of the subdivision approach presented in this section carry over to this setup. In three dimensions for example, we consider the boundary surface of the Voronoi region of each input convex site and carefully subdivide it into vertices, edges and faces. While the subdivision is more intricate than in the plane, one can harness standard tools in computational geometry to obtain a subdivision whose faces are simply connected. This surface subdivision in turn induces a subdivision of the input convex polyhedra in very much the same way as in the planar case. For lack of space, we omit further details. Notice that for higher dimensions, Voronoi diagrams for restricted types of non-point sites are available. Our first implementation target would be the case of lines in space [22], which we leave for future work.

4 Experimental results

Implementation details We implemented the planar subdivision algorithm as described in Section 3. The algorithm requires computing the combinatorial structure of the Voronoi diagram, and the critical value of each feature. We solve the first task by computing the Delaunay graph for all line segments belonging to the input polygons, using CGAL’s 2D Segment Delaunay Graphs package [24]. We restrict our attention to features of the graph for which no two defining segments belong to the same polygon and remove duplicates. For the critical values, we explicitly compute the actual curves and vertices of the Voronoi diagram and compute the minimal distance to their nearest polygonal sites. We did not use any of the optimizations mentioned in Section 3 for our experimental results. We note that more than half of the running time is used for computing the Delaunay graph and therefore the potential gain from the optimizations is limited.

For a proof of concept, we implemented the unrestricted nerve filtration described in Section 2. For the computation of critical values, we proceed in a brute-force manner, that is, we take the minimum distance over all pairs or triplets of line segments of the input polygons.

We also implemented an approximation of the barcode through point samples: Fixing some $\varepsilon > 0$, we calculate a finite point set whose Hausdorff-distance to the input is at most ε . We achieve that by placing a grid of side length $\sqrt{2}\varepsilon$ in the plane and taking as our sample the centers of all grid cells which are

Approach		Number of vertices				
		42	213	1060	2104	4217
Subdivision	Filtration time	0.052	0.26	1.442	3.103	6.523
	Persistence time	0	0	0.001	0.003	0.006
	Total time	0.052	0.26	1.443	3.106	6.529
	Filtration size	314	2102	12458	25056	50388
Unrestricted nerve	Filtration time	0.602	69.13	9920	-	-
	Persistence time	0	0.033	23.11	-	-
	Total time	0.602	69.16	9943	-	-
	Filtration size	175	20875	2604375	-	-
Point sample ($\varepsilon = 1$)	Filtration time	0.013	0.047	0.217	0.435	0.805
	Persistence time	0	0	0.001	0.001	0.003
	Total time	0.013	0.047	0.217	0.437	0.808
	Filtration size	803	2101	9021	14235	22393
Point sample ($\varepsilon = 0.5$)	Filtration time	0.023	0.07	0.312	0.594	1.045
	Persistence time	0	0	0.003	0.006	0.01
	Total time	0.024	0.07	0.315	0.6	1.055
	Filtration size	2577	6707	28273	45635	72275
Point sample ($\varepsilon = 0.1$)	Filtration time	0.304	0.765	3.22	5.106	7.975
	Persistence time	0.007	0.016	0.081	0.132	0.213
	Total time	0.310	0.781	3.3	5.238	8.188
	Filtration size	48741	120359	505833	792395	1226827

Table 1: Running time and filtration size with respect to input size. The results are averaged over 5 runs. Some results for the unrestricted nerve approach are omitted as execution did not finish within a reasonable time. Times are measured in seconds, and are highlighted in bold font.

intersected by some input polygon. We can compute this sample efficiently by taking the Minkowski sum of each polygon and a square with side length $\sqrt{2}\varepsilon$, and performing batch point location queries for a grid of points in the bounding rectangle of that polygon. We compute the alpha-filtration on the point sample, using Delaunay triangulations from CGAL’s 2D Triangulation package. We note that the size of the resulting filtration is linear with respect to the number of sampled points.

In all variants, after computing the filtration, we obtain the barcode using the PHAT software library [3].

Time analysis We compare the three approaches for several inputs of increasing sizes, and report on their running times and the size of the filtration. For generating the input, we considered a square of side length 100. We added random polygons inside the square using the following repetitive process. We randomly pick a point inside the square, and create a rectangle centered at that point with a random width and height. We then randomly select 5 points inside that rectangle and take the polygon to be their convex hull. If the polygon does not intersect any of the polygons that were previously added, we add it to our input. An illustration of an input is shown in Figure 5. All experiments were run on a 3.4GHz Intel Core i5 processor with 8GB of memory.

The experimental results are shown in Table 1. We observe that computing the filtration takes much more time than converting the filtration into a barcode. This is in sync with the common observation that despite worst-case cubical complexity, the barcode computation scales well in practice. Moreover, we get the expected result that the unrestricted nerve yields large filtrations and running times compared to the subdivision approach. In particular, for sufficiently large inputs, the time to compute the barcode from the unrestricted filtration is an order of magnitude higher than the total time in the restricted case, so even a smarter way for computing critical values will not be helpful.

Comparing the running time of the restricted nerve approach with that of the point sampling approach

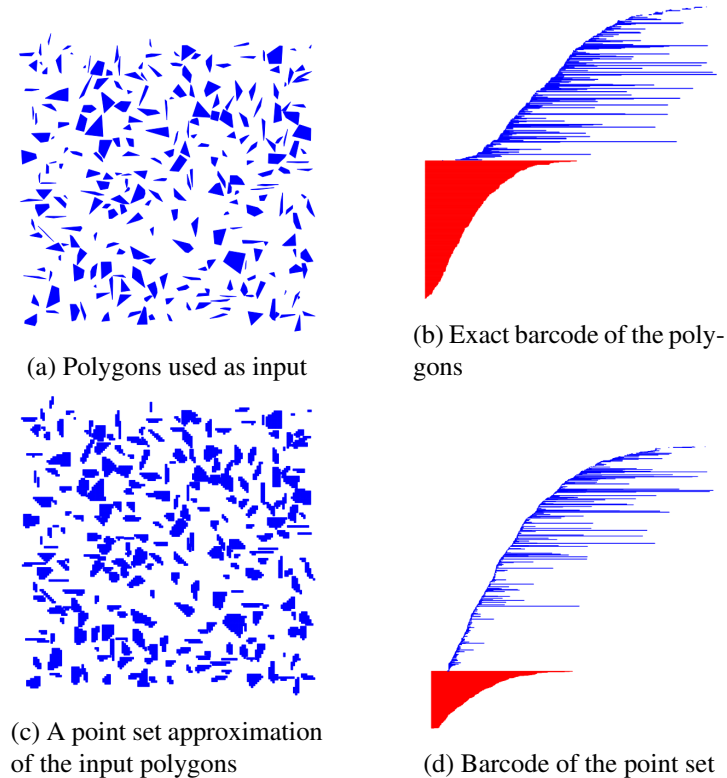


Figure 5: A comparison between an exact barcode and an approximated barcode. An illustration of polygons used as input for our experiments is shown in (a). There are 250 polygons with a total of 1060 vertices, inside a square of side length 100. The exact barcode of the polygons, computed using the subdivision method, is shown in (b). Red bars represent connected components and blue bars represent holes. It can be observed that all connected components are born at offset 0, since no connected components are created as the offset increases. When increasing the offset, connected components merge and therefore die, and holes are created and then die as they get filled. (c) shows an illustration of a point set approximation of the input polygons, with $\varepsilon = 0.5$. Each point is displayed as a pixel of size $\sqrt{2}\varepsilon$. In (d) we see the barcode of the approximation point set, which is an approximation of the exact barcode of the polygons. The approximated barcode contains many more bars compared to the exact barcode. Noise, in the form of short bars, can be observed throughout the entire barcode.

is difficult as it depends on the choice of ε . What approximation quality is reasonable generally depends on the application and the input. However, we can observe that the overhead of computing Voronoi diagrams of convex polygons instead of points is rather small, and we get the exact barcode in the same time as a “reasonable” approximation of the input. Of course, it should be admitted that our simple point-sampling approach could be significantly improved by sampling only the boundary of polygons instead, and even more by making the sample density adaptive to the *local feature size* [32] of the polygons. This however would require post-processing of the barcode to filter out topological features in the interior of polygons.

Quality of the barcodes The barcode obtained using the point sampling approach approximates the actual barcode of the input. The Stability theorem [12] ensures that the two barcodes have a distance of at most ε . Still, the question arises how much noise is introduced by the approximation. We remind the reader about our motivation to produce barcodes of shape: We want to identify offset values that minimize the number of short-lived homological features. Figure 5 shows an exact barcode and an approximated barcode for the

same input. We see that the exact barcode contains some short bars throughout the entire barcode. The approximated barcode contains many more such bars, some originating from real features in the input, and some as artifacts of the approximation. It seems (at best) very difficult to identify the real features from the approximate barcode, which speaks in favor of using the exact approach in such types of applications.

References

- [1] F. Aurenhammer and R. Klein. Chapter 5 - Voronoi diagrams. In J.-R. Sack and J. Urrutia, editors, *Handbook of Computational Geometry*, pages 201 – 290. North-Holland, 2000.
- [2] U. Bauer, M. Kerber, and J. Reininghaus. Clear and compress: Computing persistent homology in chunks. In *Topological Methods in Data Analysis and Visualization III*. Springer, 2014.
- [3] U. Bauer, M. Kerber, J. Reininghaus, and H. Wagner. Phat - persistent homology algorithms toolbox. In *4th International Congress of Mathematical Software*, 2014.
- [4] S. Biasotti, D. Giorgi, M. Spagnuolo, and B. Falcidieno. Reeb graphs for shape analysis and applications. *Theoretical Computer Science*, 392:5 – 22, 2008.
- [5] G. Carlsson, A. Zomorodian, A. Collins, and L. Guibas. Persistence barcodes for shapes. In *Proceedings of the 2004 Symposium on Geometry Processing*, pages 124–135, 2004.
- [6] J. Chan, G. Carlsson, and R. Rabadan. Topology of viral evolution. *Proceedings of the National Academy of Sciences*, 2013.
- [7] F. Chazal, D. Cohen-Steiner, M. Glisse, L. Guibas, and S. Oudot. Proximity of persistence modules and their diagrams. In *Proceedings of the 25th ACM Symposium on Computational Geometry*, pages 237–246, 2009.
- [8] F. Chazal, V. de Silva, M. Glisse, and S. Oudot. The structure and stability of persistence modules. *arXiv 1207.3674*, 2012.
- [9] F. Chazal and S. Oudot. Towards persistence-based reconstruction in Euclidean spaces. In *Proceedings of the Twenty-fourth Annual Symposium on Computational Geometry*, pages 232–241, 2008.
- [10] C. Chen and M. Kerber. An output-sensitive algorithm for persistent homology. *Computational Geometry: Theory and Applications*, 46(4):435–447, 2013.
- [11] M. Chung, P. Bubenik, and P. Kim. Persistence diagrams of cortical surface data. In *Information Processing in Medical Imaging*, pages 386–397, 2009.
- [12] D. Cohen-Steiner, H. Edelsbrunner, and J. Harer. Stability of persistence diagrams. *Discrete & Computational Geometry*, 37:103–120, 2007.
- [13] D. Cohen-Steiner, H. Edelsbrunner, and J. Harer. Extending persistence using Poincaré and Lefschetz duality. *Foundations of Computational Mathematics*, 9:79–103, 2009.
- [14] M. de Berg, M. van Kreveld, M. Overmars, and O. Schwarzkopf. *Computational Geometry: Algorithms and Applications*. Springer, 2nd edition, 2000.
- [15] C. Delfinado and H. Edelsbrunner. An incremental algorithm for betti numbers of simplicial complexes. In *Proceedings of the ninth Annual Symposium on Computational Geometry*, pages 232–239, 1993.

- [16] H. Edelsbrunner and J. Harer. *Computational Topology. An Introduction*. American Mathematical Society, 2010.
- [17] H. Edelsbrunner, D. Letscher, and A. Zomorodian. Topological persistence and simplification. *Discrete & Computational Geometry*, 28(4):511–533, 2002.
- [18] B. Di Fabio and C. Landi. Persistent homology and partial similarity of shapes. *Pattern Recognition Letters*, 33(11):1445–1450, 2012.
- [19] S. Fortune. Voronoi diagrams and Delaunay triangulations. In Jacob E. Goodman and Joseph O’Rourke, editors, *Handbook of Discrete and Computational Geometry*, chapter 20, pages 377–388. CRC Press LLC, 1997.
- [20] A. Hatcher. *Algebraic Topology*. Cambridge University Press, 2001.
- [21] M. Held. Vroni and arcvroni: Software for and applications of Voronoi diagrams in science and engineering. In *Voronoi Diagrams in Science and Engineering*, pages 3–12, 2011.
- [22] M. Hemmer, O. Setter, and D. Halperin. Constructing the exact Voronoi diagram of arbitrary lines in three-dimensional space - with fast point-location. In *European Symposium on Algorithms*, pages 398–409, 2010.
- [23] S. Hornus and J-D. Boissonnat. An efficient implementation of Delaunay triangulations in medium dimensions. Technical report, INRIA No. 6743, 2008.
- [24] M. Karavelas. 2D segment Delaunay graphs. In *CGAL User and Reference Manual*. CGAL Editorial Board, 4.4 edition, 2000.
- [25] M. Karavelas and M. Yvinec. The Voronoi diagram of planar convex objects. In *European Symposium on Algorithms*, pages 337–348, 2003.
- [26] K. Kedem, R. Livne, J. Pach, and M. Sharir. On the union of jordan regions and collision-free translational motion amidst polygonal obstacles. *Discrete & Computational Geometry*, 1:59–70, 1986.
- [27] J. Matouek, M. Sharir, and E. Welzl. A subexponential bound for linear programming. *Algorithmica*, 16(4-5):498–516, 1996.
- [28] V. Milenkovic. Robust construction of the Voronoi diagram of a polyhedron. In *Proceedings of the 5th Canadian Conference on Computational Geometry*, pages 473–478, 1993.
- [29] N. Milosavljević, D. Morozov, and P. Škraba. Zigzag persistent homology in matrix multiplication time. In *Proceedings of the 27th Annual Symposium on Computational Geometry*, pages 216–225, 2011.
- [30] J.R. Munkres. *Elements of algebraic topology*. Westview Press, 1984.
- [31] S. Pion and M. Teillaud. 3D triangulations. In *CGAL User and Reference Manual*. CGAL Editorial Board, 4.4 edition, 2000.
- [32] J. Ruppert. A Delaunay refinement algorithm for quality 2-dimensional mesh generation. *Journal of Algorithms*, 18(3):548 – 585, 1995.
- [33] J. Shewchuk. Delaunay refinement algorithms for triangular mesh generation. *Computational Geometry: Theory and Applications*, 22(1-3):21–74, 2002.

- [34] P. Skraba, M. Ovsjanikov, F. Chazal, and L. Guibas. Persistence-based segmentation of deformable shapes. In *Computer Vision and Pattern Recognition Workshops*, pages 2146–2153, 2010.
- [35] O. Stava, J. Vanek, B. Benes, N. Carr, and R. Mech. Stress relief: improving structural strength of 3d printable objects. *ACM Transactions on Graphics*, 31(4):48, 2012.
- [36] R. van de Weygaert, G. Vegter, H. Edelsbrunner, B. Jones, P. Pranav, C. Park, W. Hellwing, B. Eldering, N. Kruihof, E. Bos, J. Hidding, J. Feldbrugge, E. ten Have, M. van Engelen, M. Caroli, and M. Teilaud. Alpha, betti and the megaparsec universe: On the topology of the cosmic web. In *Transactions on Computational Science XIV*, LNCS 6970, pages 60–101. Springer, 2011.
- [37] C.K. Yap, V. Sharma, and Jyh-Ming Lien. Towards exact numerical Voronoi diagrams. In *Voronoi Diagrams in Science and Engineering*, pages 2–16, 2012.
- [38] M. Yvinec. 2D triangulations. In *CGAL User and Reference Manual*. CGAL Editorial Board, 4.4 edition, 2000.
- [39] A. Zomorodian and G. Carlsson. Computing persistent homology. *Discrete & Computational Geometry*, 33:249–274, 2005.

A Proof of Theorem 10: Tisk-theory

The main goal of this section is to give a proof of Theorem 10. On the way, we will also give arguments that complete the proofs of Lemma 5 and Lemma 7.

For that, we first slightly abstract from offsets and Voronoi regions, and define a class of objects that includes all of them.

Definition 11. A piecewise-algebraic path is a simple path in \mathbb{R}^2 which consists of a finite number of arcs, where each arc is a semi-algebraic curve. A piecewise-algebraic loop is such a path that is homeomorphic to a circle. A set $D \subset \mathbb{R}^2$ is a bounded tisk if D is the closed bounded region induced by a piecewise-algebraic loop. D is an unbounded tisk if it is the closed region induced by an unbounded piecewise-algebraic path. Two tisks A, B with boundary curves a, b , are called interior-disjoint if $A \cap B = a \cap b$.

We remark that every Voronoi region as well as any restricted offset is a tisk, because their boundaries consist of line segments, circular arcs, and parabolic arcs.

We consider the intersection of two interior-disjoint tisks A and B . Let a and b denote the boundary curves of A and of B respectively. The curve a is partitioned into interior-disjoint segments, alternating between segments that belong to $a \cap b$ (such a segment may degenerate to a point), and segments that belong to $a \setminus b$. The symmetric property holds for b . The partition points are denoted by V_{ab} . Note that V_{ab} is empty if and only if A and B are non-intersecting, or both are unbounded and their union is the whole space. Note also that by choosing an arbitrary orientation on a or on b , we can define a total order on V_{ab} . These definitions are illustrated in Figure 6.

Definition 12. The connected components of $\text{Clos}(\mathbb{R}^2 \setminus A \cup B)$ are called complementary regions of (A, B) . A surrounded region is a complementary region that is bounded.

Note that this definition of surrounded regions agrees with the definition given in Section 3 for the special case that tisks are Voronoi regions. Every surrounded region is a tisk whose boundary loop involves two consecutive points of V_{ab} connected by one segment in $a \setminus b$ and one segment in $b \setminus a$. An unbounded complementary region might or might not be a tisk, depending on whether A and B are bounded. For instance, if both A and B are bounded, there is only one unbounded complementary region, and it is the

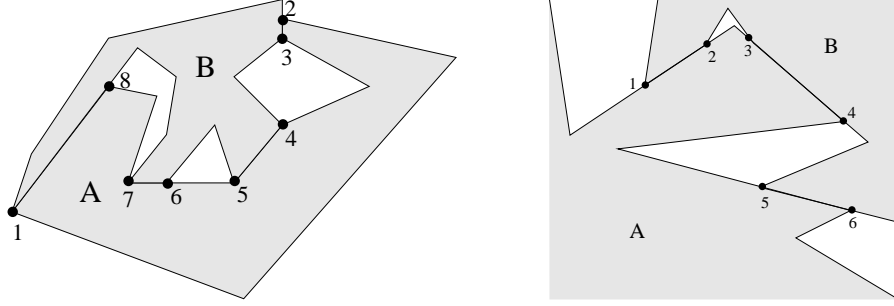


Figure 6: Examples of interior-disjoint intersecting tasks. On the left, their complement is composed into three surrounded regions and one unbounded region. On the right, the complement is composed into two surrounded regions and two unbounded regions. The points on V_{ab} are highlighted, and a possible ordering is given.

complement of a task. We can easily see that every surrounded region of (A, B) contains exactly two points of V_{ab} . Every unbounded complementary region contains one or two points of V_{ab} ; more precisely, if there is only one unbounded region, it contains two points of V_{ab} , and if there are two such regions, they contain one point of V_{ab} each. See again Figure 6 for illustrations of these concepts.

Lemma 13. *Assume that $a \cap b = A \cap B$ is non-empty. Then, it is contractible if and only if (A, B) does not induce a surrounded region.*

Proof. “ \Leftarrow ” follows directly from the definition: Assume that $a \cap b$ is non-contractible. Then, $a \cap b$ decomposes into at least two connected components, and there exist consecutive points $v, v' \in V_{ab}$ which are connected by segments in $a \setminus b$ and $b \setminus a$. The task enclosed by this loop is a surrounded region.

For “ \Rightarrow ”, contractibility implies that V_{ab} consists of exactly two points, and both lie in the unbounded complementary region, so there are no points in V_{ab} left to form a surrounded region. \square

Next, we consider a collection \mathcal{S} of pairwise interior-disjoint tasks. We assume generic position, that is, no more than three tasks intersect in a common point. Three tasks A, B, C of \mathcal{S} with boundary curves a, b, c intersect in at most two points; this follows from the observation that $a \cap b \cap c \subseteq V_{ab}$ (because any intersection of c in the interior of a segment of $a \cap b$ would imply that C is not interior disjoint to A or B), combined with the fact that C must be contained in some complementary region of (A, B) , each of which contains at most 2 points of V_{ab} .

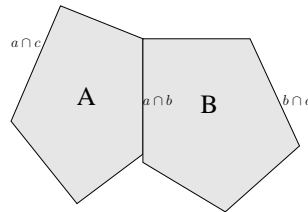


Figure 7: Illustration of the proof of Lemma 14. The set C has to be bounded by the outer cycle, which implies that either C has an inner hole (contradicting the task-property) or it contains A and B (contradicting interior-disjointness).

Lemma 14. *If any pair in \mathcal{S} is empty or contractible, then every triple in \mathcal{S} is empty or a single point.*

Proof. Consider a triple A, B, C with boundary curves a, b, c and non-empty intersection. We assume that $a \cap b$ is contractible. That implies that $|V_{ab}| \leq 2$. Wlog, we can assume that $|V_{ab}| = 2$, because otherwise, $a \cap b \cap c \subseteq V_{ab}$ contains at most one point and we are done. Let $V_{ab} = \{v_1, v_2\}$. There exists a segment of $a \cap b$ connecting v_1 to v_2 . Assume first that A is unbounded: then, there exist two segments in $a \setminus b$, one emanating at v_1 , one at v_2 . Since c cannot intersect a in the interior of $a \cap b$, $a \cap c$ must be a subset of $a \setminus b$. However, $a \cap c$ contains v_1 and v_2 , therefore, it consists of at least two connected components. This is a contradiction to the assumption that $a \cap c$ is contractible. A symmetric argument implies that B must be bounded.

We are left with the case that both A and B are bounded. Then $a \setminus b$ and $b \setminus a$ are segments that connect v_1 and v_2 . Since $a \cap c$ and $b \cap c$ are contractible, it follows that the loop of c is the union of these segments. However, that loop encloses both A and B , which contradicts the interior disjointness of the tasks. \square

We can apply this Lemma to complete the proof of Lemma 5 (for the special case of Voronoi regions) and the proof of Lemma 7 (for the special case of restricted offsets).

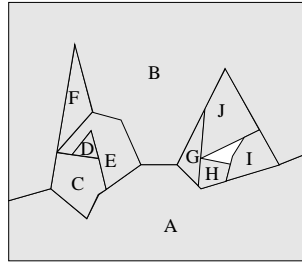


Figure 8: A and B induce two surrounded regions. The left one has the four members C, D, E, F , the right one the four members G, H, I, J . The left region is filled but not simple, because C and E induce a nested surrounded region. This nested region, in turn, is filled and simple. The right region is simple, but not filled; note that the uncovered hole is not a surrounded region.

For the upcoming definitions, see also Figure 8. For a surrounded region R induced by A and B , we call a task S in \mathcal{S} a *member* of R if $S \subseteq R$. Note that a surrounded region might have an arbitrary number of members, including no member at all. We let M_R denote the set of members of R , and $M_R^{\text{ext}} := M_R \cup \{A, B\}$ the set of *extended members*. We call a surrounded region R *filled*, if the union of its members equals R (in this case, R must have at least one member). We define a *simple surrounded region* of \mathcal{S} to be a surrounded region such that no other surrounded region is contained in it.

The following property will be of special importance; we will refer to it as the “guarding principle”.

Lemma 15. *For a collection of tasks \mathcal{S} in generic position and a surrounded region R , there is no intersection of a member of R with an element of $\mathcal{S} \setminus M_R^{\text{ext}}$.*

Proof. Let R be induced by the tasks A and B , and let a, b their boundaries. Assume by contradiction the existence of such an intersection. Then, there must be a task $C \in M_R^{\text{ext}}$ that intersects the boundary of R . It is easy to see that this intersection cannot take place within $a \setminus b$ (because A and C are interior-disjoint and a is simple), and the same way for $b \setminus a$. It follows that C intersects the boundary of R at $v \in a \cap b$. However, by assumption, C intersects a fourth task $D \in M_R$ at point v . So, v is an intersection of four tasks which contradicts our genericity assumption. \square

An equivalent statement is that if R is induced by A and B , the set $\{A, B\}$ constitutes a separator in $\text{Nrv } \mathcal{S}$, separating the elements within R and the elements outside of R .

We now state the first main theorem that will be needed for the proof of Theorem 10. As usual, we let $|\mathcal{S}|$ denote the underlying space of \mathcal{S} , which is the union over all tasks in \mathcal{S} .

Theorem 16. *Let \mathcal{S} be a collection of tisks in generic position such that every surrounded region is filled. Then $H_1(\text{Nrv}(\mathcal{S})) = H_1(|\mathcal{S}|)$.*

The idea of the proof is to “clear out” surrounded regions one after the other by removing the members within a surrounded region and charging the surrounded region to one of the two tisks that surround it. These operations do not change the underlying space. Moreover, as we will show, there cannot be any non-trivial 1-homology in the nerve of a surrounded region. Finally, by the guarding principle, removing the member of a surrounded region does not affect the connectivity of remaining tisks. These properties will be enough to ensure the isomorphism. We give the details of the single steps next.

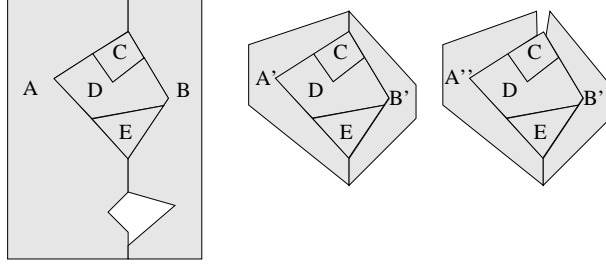


Figure 9: Illustration of the transformation in the proof of Lemma 17. On the left, we see a simple surrounded and filled region R with members C, D, E . In the middle, we shrink A and B to local neighborhoods around R , ignoring possible further surrounded regions. On the right, we disconnect one of the two intersections of A' and B' without disconnecting (A', C) or (B', C) . The obtained subdivision has only contractible intersections.

Lemma 17. *Let R be a surrounded region that is simple and filled. Then, $H_1(\text{Nrv}M_R^{\text{ext}}) = 0$.*

Proof. Let the surrounded region R be induced by (A, B) , and we set $M := M_R^{\text{ext}}$ for notational convenience. First of all, note that we can restrict A and B to a local neighborhood around R without changing the nerve of M . Formally, replace A by A' , which is the intersection of A with an ε -offset of R (for $\varepsilon > 0$ small enough), and same for B . We set $M' := M_R \cup \{A', B'\}$. Clearly, $\text{Nrv}M = \text{Nrv}M'$. See Figure 9 (middle).

We want to prove the claim using the Nerve theorem; however, the intersection of A' and B' is non-contractible. We perform another local surgery to avoid this problem: Let v be one of the two intersection points of $A \cap B \cap R$, and let $C \in M_R$ be the member adjacent to this point (C exists because R is filled, and C is unique because only three tisks intersect in one point). We can separate A' and B' locally around v with a small distance while leaving the pairwise intersections with C intact (again, because we assume non-degeneracy, $A' \cap C$ is a non-degenerate segment). Let A'', B'' be the replacements, and let $M'' := M_R \cup \{A'', B''\}$; note that A'' and B'' are still connected at the second intersection point of $A \cap B \cap R$; it follows that $\text{Nrv}M''$ has the same edges of $\text{Nrv}M$; in fact, the nerves are the same, except that the triangle $ABC \in \text{Nrv}M$ might or might not have a counterpart in $\text{Nrv}M''$. See Figure 9 (right).

It is enough to show that $H_1(\text{Nrv}M'') = 0$. Any pair of tisks in M'' has a non-contractible intersection: we explicitly constructed A'' and B'' to have non-contractible intersection, and if any pair in M'' had a non-contractible intersection, it would introduce a surrounded region inside R which contradicts the assumption that R is simple. By Lemma 14, this implies M'' is a good partition and the Nerve theorem applies. So, $\text{Nrv}M''$ is homotopically equivalent to $|M''|$, which is a topological disk because R is filled. It follows that $H_1(\text{Nrv}M'') = 0$, as required. \square

Recall that M_R is the set of member of a surrounded region R and let \mathcal{S}_R denote the set $\mathcal{S} \setminus M_R$. We define a map

$$\phi_R: \mathcal{S} \rightarrow \mathcal{S}_R$$

mapping each member of R to A , and any other task to itself. We have the induced simplicial map

$$\text{Nrv}(\mathcal{S}) \rightarrow \text{Nrv}(\mathcal{S}_R),$$

which maps a simplex $\sigma = (S_0, \dots, S_k) \in \text{Nrv}(\mathcal{S})$ with $S_i \in \mathcal{S}$ to the simplex $(\phi_R(S_0), \dots, \phi_R(S_k))$. Slightly abusing notation, we also write ϕ_R for this map on the nerve level. Note that $\phi_R(S_i)$ might be equal to $\phi_R(S_j)$, so ϕ_R may map a k -simplex to an ℓ -simplex with $\ell \leq k$.

We need to argue that ϕ_R is well-defined, that is, $\phi_R(\sigma) \in \text{Nrv}(\mathcal{S}_R)$. For that, observe that if σ does not contain any member of R , it stays in the nerve when removing R , and $\phi_R(\sigma) = \sigma$. On the other hand, if σ contains any member of R , it can only contain extended members of R by the guarding principle. Therefore, $\phi_R(\sigma) = (A)$ or $\phi_R(\sigma) = (A, B)$, and both are in $\text{Nrv}(\mathcal{S}_R)$.

Being a simplicial map, ϕ_R induces a map

$$\phi_R^* : H_1(\text{Nrv}(\mathcal{S})) \rightarrow H_1(\text{Nrv}(\mathcal{S}_R))$$

of homology groups. We show that this map is an isomorphism if R is simple and filled.

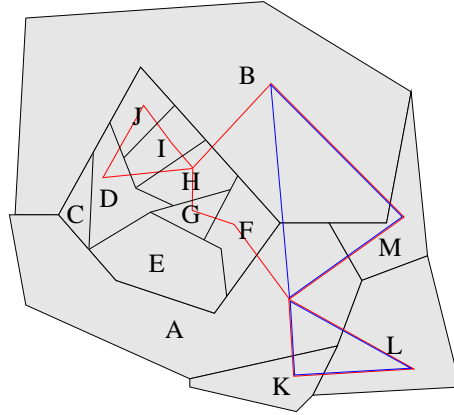


Figure 10: Illustration of the transformation in the proof of Lemma 18. A and B induce a simple and filled surrounded region R with members C, D, \dots, J . The red curve represents a cycle c in the $\text{Nrv}(\mathcal{S})$: the edges in the cycle are defined by the intersections that the curve crosses. In this example, the cycle consists of three loops, each of a different type: The loop $DJ + JI + IH + HD$ consists of extended members of R (type (1)) is transformed into the trivial cycle. The loop $AK + KL + LA$ consists of elements of $\mathcal{S} \setminus M_R$ and is thus preserved. The third loop $AF + FG + GH + HB + BM + MA$ is of mixed type. The path $AF + FG + GH + HB$ consists only of extended members and is replaced by AB . The blue curve shows the resulting cycle c' .

Lemma 18. *If a surrounded region R is simple and filled, the map ϕ_R^* is an isomorphism.*

Proof. $\mathcal{S}_R \subseteq \mathcal{S}$ implies immediately that the map is surjective. The *support* of a d -chain is the union of all vertices that are boundary vertices of at least one simplex in the chain. For injectivity, we claim for any 1-cycle c in $\text{Nrv}(\mathcal{S})$, there is an homologous cycle that is only supported by vertices in \mathcal{S}_R . Indeed, this statement implies injectivity: Assume that $[c_1], [c_2] \in H_1(\text{Nrv}(\mathcal{S}))$ are such that $\phi_R^*([c_1]) = \phi_R^*([c_2])$. Then, we can replace the representatives c_1, c_2 by c'_1, c'_2 supported by \mathcal{S}_R . Since ϕ_R is the identity on \mathcal{S}_R , we have

$$[c_1] = [c'_1] = \phi_R^*([c'_1]) = \phi_R^*([c'_2]) = [c'_2] = [c_2].$$

To prove the remaining claim, we fix a 1-cycle c in $\text{Nrv}(\mathcal{S})$. c decomposes into a collection of “simple” loops, that is, loops in which every vertex is traversed only once. There are three possibilities for such a

loop: Its support lies (1) entirely in M_R^{ext} , (2) entirely in $\mathcal{S} \setminus M_R$, or (3) contains elements of both M_R and $\mathcal{S} \setminus M_R^{\text{ext}}$. In the latter case, both A and B must be in the support (because A and B are the only entry points into M_R^{ext} from the outside by the guarding principle), and the loop splits into two parts at A and B , one that is supported entirely by M_R^{ext} and one entirely supported by $\mathcal{S} \setminus M_R$. See also Figure 10.

We construct c' from c as follows: Iterating over all loops of c , we remove loops of type (1), and leave loops of type (2) unchanged. For loops of type (3), we replace the subpath supported by M_R^{ext} with the edge AB . Note that after these replacements, c' is indeed supported by vertices in $\mathcal{S} \setminus M_R = \mathcal{S}_R$.

It remains to prove that $[c] = [c']$. We show that every loop transformation yields a homologous cycle. For type (1), note that the loop is a cycle in $\text{Nrv}M_R^{\text{ext}}$. By Lemma 17, such a cycle is null-homologous, so removing the loop does not change the homology type. For type (2), there is nothing to do. For type (3), consider the subpath of the loop inside M_R^{ext} ; if it consists only of the edge AB , the loop remains unchanged. Otherwise, the concatenation of the path with the edge AB induces a cycle in $\text{Nrv}(M_R^{\text{ext}})$. Using Lemma 17, the loop is null-homologous, thus we can one path by the other without changing the homotopy type. \square

We complete the proof of the first main statement next.

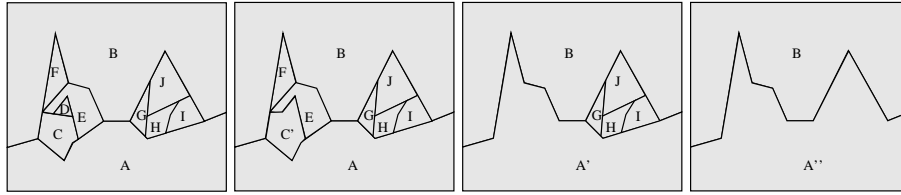


Figure 11: Illustration of the transformation in the proof of Theorem 19. The situation is a slight variation of Figure 8. We have three surrounded regions, two induced by (A, B) , and one by (C, E) and they are all filled. We first remove the simple surrounded region induced by (C, E) . We charge the hole when removing the region to one of the surrounds, say C , transforming it into C' (2nd figure). This turns the left surrounded region of (A, B) simple as well. We perform the same operation twice and transform A into A' (3rd figure) and finally into A'' (4th figure). After that, the collection has no more surrounded region.

Theorem 19. *Let \mathcal{S} be a collection of tasks in generic position such that every surrounded region is filled. Then $H_1(\text{Nrv}(\mathcal{S})) = H_1(|\mathcal{S}|)$.*

Proof. We assume that \mathcal{S} induces at least one surrounded region. In that case, it must also induce a simple one, and we let R denote it and (A, B) be the pair in \mathcal{S} that causes R . By Lemma 18, because R is filled, we have $H_1(\text{Nrv}(\mathcal{S})) = H_1(\text{Nrv}(\mathcal{S}_R))$. Now, we set $A' := A \cup R$ and consider \mathcal{S}'_R , where we replace A with A' (Figure 11). We note that $\text{Nrv}\mathcal{S}'_R = \text{Nrv}\mathcal{S}_R$, because the extension of A did not introduce any new connection. This implies in particular that $H_1(\text{Nrv}(\mathcal{S})) = H_1(\text{Nrv}(\mathcal{S}'_R))$. Moreover, $|\mathcal{S}'_R| = |\mathcal{S}|$, because A' occupies exactly the space that has been occupied by the members of R . Finally, the surrounded regions of \mathcal{S}'_R are equal to the surrounded regions of \mathcal{S} , except that the simple region R was removed. In other words, representing the surrounded region by a forest where R_1 is an ancestor of R_2 if $R_1 \subseteq R_2$, the surrounding forest of \mathcal{S}'_R equals the surrounding forest of \mathcal{S} with one leaf removed.

By iterating this construction, we find a collection \mathcal{S}^* of tasks such that $H_1(\text{Nrv}(\mathcal{S})) = H_1(\text{Nrv}(\mathcal{S}^*))$, $|\mathcal{S}| = |\mathcal{S}^*|$, and \mathcal{S} does not induce any surrounding region. The last property, however, implies that all pairwise intersections are contractible. Therefore, Lemma 14 applies and we can use the Nerve Theorem, which states that $\text{Nrv}(\mathcal{S}^*)$ is homotopically equivalent to $|\mathcal{S}^*|$. In particular, their homology groups are isomorphic. Putting everything together, we have that

$$H_1(\text{Nrv}(\mathcal{S})) = H_1(\text{Nrv}(\mathcal{S}^*)) = H_1(|\mathcal{S}^*|) = H_1(|\mathcal{S}|)$$

\square

Finally, we consider filtrations of tasks according to the following definition.

Definition 20. A family of tasks $(S^\alpha)_{\alpha \geq 0}$ is called a task-inclusion if $S^\alpha \subseteq S^{\alpha'}$ for $\alpha \leq \alpha'$. A collection of task-inclusions $(\mathcal{S}^\alpha)_{\alpha \geq 0} = (\{S_1^\alpha, \dots, S_N^\alpha\})_{\alpha \geq 0}$ is called a task-filtration. For each $\alpha \geq 0$, it defines a collection of tasks at scale α . A task-filtration is called sane if for every α , the collection of tasks is interior-disjoint, in generic position, and all its surrounded regions are filled.

For a sane task-filtration $(\mathcal{S}^\alpha)_{\alpha \geq 0}$, Theorem 19 establishes an isomorphism between the first homology group of $\text{Nrv}(\mathcal{S}^\alpha)$ and $|\mathcal{S}^\alpha|$ for every $\alpha > 0$. On the other hand, for $\alpha_1 \leq \alpha_2$, we have natural inclusions from $|\mathcal{S}^{\alpha_1}|$ to $|\mathcal{S}^{\alpha_2}|$ as well as inclusions on their nerves. We show next that these inclusions commute with the isomorphisms.

Theorem 21. For a sane task-filtration $(\mathcal{S}^\alpha)_{\alpha \geq 0}$ and $\alpha_1 \leq \alpha_2$, the diagram

$$\begin{array}{ccc} H_1(|\mathcal{S}^{\alpha_1}|) & \hookrightarrow & H_1(|\mathcal{S}^{\alpha_2}|) \\ \psi^* \uparrow & & \psi^* \uparrow \\ H_1(\text{Nrv}(\mathcal{S}^{\alpha_1})) & \hookrightarrow & H_1(\text{Nrv}(\mathcal{S}^{\alpha_2})) \end{array}$$

commutes, where ψ^* is the isomorphism as constructed in Theorem 19.

Proof. The proof is lengthy and requires us to study the isomorphisms induced by the Nerve theorem, in a similar spirit as in [9]. We let $R_1^{(1)}, \dots, R_{h_1}^{(1)}$ denote the surrounded regions of \mathcal{S}^{α_1} and $R_1^{(2)}, \dots, R_{h_2}^{(2)}$ those of \mathcal{S}^{α_2} . Clearly, $h_1 \leq h_2$ and we can label the surrounded regions such that $R_i^{(1)} = R_i^{(2)}$ for $1 \leq i \leq h_1$. Recall that in the construction of ψ^* (Theorem 19), we repeatedly remove tasks from surrounded regions and charge their area to one of its surrounding tasks. After removing all surrounded regions, we arrive at a collection $(\mathcal{S}^{\alpha_i})^*$ from \mathcal{S}^{α_i} with the same underlying space, and a simplicial map

$$\phi_i : \text{Nrv}(\mathcal{S}^{\alpha_i}) \rightarrow \text{Nrv}((\mathcal{S}^{\alpha_i})^*),$$

which induces an isomorphism ϕ_i^* between the 1-st homology groups. Moreover, because $(\mathcal{S}^{\alpha_i})^*$ has no surrounded regions, the Nerve theorem defines an isomorphism

$$\theta_i^* : H_i(\text{Nrv}((\mathcal{S}^{\alpha_i})^*)) \rightarrow H_i(|(\mathcal{S}^{\alpha_i})^*|).$$

Finally, there is a natural simplicial map

$$\gamma : \text{Nrv}((\mathcal{S}^{\alpha_1})^*) \rightarrow \text{Nrv}((\mathcal{S}^{\alpha_2})^*)$$

where we map a task that is not surrounded at α_1 , but surrounded at α_2 to one of its surrounding tasks (in other words, γ can be seen as the restriction of ϕ_2 to $\text{Nrv}((\mathcal{S}^{\alpha_1})^*)$). Putting everything together, we have the following diagram

$$\begin{array}{ccc} H_1(|\mathcal{S}^{\alpha_1}|) & \xrightarrow{\subseteq} & H_1(|\mathcal{S}^{\alpha_2}|) & (2) \\ \parallel & & \parallel & \\ H_1(|(\mathcal{S}^{\alpha_1})^*|) & \xrightarrow{\subseteq} & H_1(|(\mathcal{S}^{\alpha_2})^*|) & \\ \theta_1^* \uparrow & & \theta_2^* \uparrow & \\ H_1(\text{Nrv}((\mathcal{S}^{\alpha_1})^*)) & \xrightarrow{\gamma^*} & H_1(\text{Nrv}((\mathcal{S}^{\alpha_2})^*)) & \\ \phi_1^* \uparrow & & \phi_2^* \uparrow & \\ H_1(\text{Nrv}(\mathcal{S}^{\alpha_1})) & \xrightarrow{\subseteq} & H_1(\text{Nrv}(\mathcal{S}^{\alpha_2})) & \end{array}$$

where \subseteq means that the corresponding map is induced by inclusion. We show that every square in this diagram commutes. This is immediately clear for the upper square from the top. For the lower square, we observe that the corresponding diagram on the simplicial level already commutes, by definition of γ .

For the middle square, we need to investigate the isomorphism θ_i^* in more detail. (Note that we cannot apply Theorem 2 because γ^* is not induced by inclusion) We still want to follow the approach from [9, Lemma 3.4], [20, Sec. 4G]. A technical difficulty is that these results require *open* covers of the underlying space, while we cover with closed spaces. However, we can just replace any task in $(\mathcal{S}^{\alpha_i})^*$ by an offset of itself with a sufficiently small ε -value and restrict the offset to the underlying space. This yields an open cover \mathcal{U}^{α_i} , with same underlying space and the same nerve as $(\mathcal{S}^{\alpha_i})^*$ – this is possible because we assume our tasks to be bounded by finitely many algebraic sets which rules out pathological cases where tasks come arbitrary close to each other without intersecting. With that, we have the diagram

$$\begin{array}{ccc}
H_1(|(\mathcal{S}^{\alpha_1})^*|) & \xrightarrow{\subseteq} & H_1(|(\mathcal{S}^{\alpha_2})^*|) \\
\parallel & & \parallel \\
H_1(|\mathcal{U}^{\alpha_1}|) & \xrightarrow{\subseteq} & H_1(|\mathcal{U}^{\alpha_2}|) \\
\theta_1^* \uparrow & & \theta_2^* \uparrow \\
H_1(\text{Nrv}(\mathcal{U}^{\alpha_1})) & \xrightarrow{\gamma^*} & H_1(\text{Nrv}(\mathcal{U}^{\alpha_2})) \\
\parallel & & \parallel \\
H_1(\text{Nrv}((\mathcal{S}^{\alpha_1})^*)) & \xrightarrow{\gamma^*} & H_1(\text{Nrv}((\mathcal{S}^{\alpha_2})^*))
\end{array}$$

where the upper and lower square obviously commute, and we only need to show that the middle square commutes. Set $X_i := |\mathcal{U}^{\alpha_i}|$ for convenience, and let $U_1^{(i)}, \dots, U_{n_i}^{(i)}$ denote the elements in the open cover \mathcal{U}^{α_i} . Let Δ^{n_i-1} denote the standard simplex of dimension $n_i - 1$. We define a space $\Delta X_i \subseteq X_i \times \Delta^{n_i-1}$ as follows: Any non-empty subset $\sigma \subset \{1, \dots, n_i\}$ defines a simplex $[\sigma]$ of Δ^{n_i-1} choosing the corresponding vertex set. Also, σ induces a (possibly empty) set $U_\sigma^{(i)} = \bigcap_{j \in \sigma} U_j^{(i)}$. We set

$$\Delta X_i := \bigcup_{\emptyset \neq \sigma \subseteq \{1, \dots, n_i\}} U_\sigma^{(i)} \times [\sigma].$$

Our next goal is to define a map that connects ΔX_1 and ΔX_2 . Note first that $\gamma: \text{Nrv}((\mathcal{S}^{\alpha_1})^*) \rightarrow \text{Nrv}((\mathcal{S}^{\alpha_2})^*)$ is defined through a vertex map from one nerve to the other, by identifying surrounded tasks with one of their surrounders. By assigning indices and tasks, γ can be encoded as a map $\gamma: \{1, \dots, n_1\} \rightarrow \{1, \dots, n_2\}$. Note that the individual tasks are only growing when surrounded regions are eliminated; therefore, we have that $U_k^{(1)} \subseteq U_{\gamma(k)}^{(2)}$. γ also extends to a surjective map from Δ^{n_1-1} to Δ^{n_2-1} in a natural way, and we have that $U_\sigma^{(1)} \subseteq U_{\gamma(\sigma)}^{(2)}$. Therefore, the map

$$\xi: \Delta X_1 \rightarrow \Delta X_2$$

which maps (x, v) to $(x, \gamma(v))$ is well-defined.

Finally, let Γ_i denote the barycentric subdivision of $\text{Nrv}\mathcal{U}^{\alpha_i}$ and note that γ also extends to a map $\gamma': \Gamma_1 \rightarrow \Gamma_2$ in a natural way. Now we consider the following diagram

$$\begin{array}{ccc}
X_1 & \hookrightarrow & X_2 \\
p_1 \uparrow & & p_2 \uparrow \\
\Delta X_1 & \xrightarrow{\xi} & \Delta X_2 \\
q_1 \downarrow & & q_2 \downarrow \\
\Gamma_1 & \xrightarrow{\gamma} & \Gamma_2
\end{array}$$

where p_i is the natural projection from Δ_i to X_i and q_i is the map obtained by contracting every $U_\sigma^{(i)}$ to a single point, say x_0 . Both squares commute: For the first square, this is immediately clear, because a point $(x, v) \in \Delta X_1$ is mapped to $x \in X_2$, regardless of how to follow the diagram. For the second square, let $(x, v) \in \Delta X_1$ and note that $q_2(\xi(x, v)) = q_2(x, \gamma'(v)) = (x_0, \gamma'(v))$ and $\gamma'(q_1(x, v)) = \gamma'(x_0, v) = (x_0, \gamma'(v))$.

We consider the diagram

$$\begin{array}{ccc}
C_k(\Gamma_1) & \xrightarrow{\gamma'_p} & C_k(\Gamma_2) \\
h_1 \uparrow & & h_2 \uparrow \\
C_k(\text{Nrv}\mathcal{U}^{\alpha_1}) & \xrightarrow{\gamma_p} & C_k(\text{Nrv}\mathcal{U}^{\alpha_2})
\end{array}$$

of k -chain groups, where γ_p, γ'_p are chain maps for dimension p induced by γ and γ' (see [30, p.72]). h_i is the chain map defined by mapping a k -simplex $\sigma \in \text{Nrv}\mathcal{U}^{\alpha_1}$ to the chain of k -simplices that are incident to the vertex $\hat{\sigma}$ representing σ in Γ_i . It is again straight-forward to see that the diagram commutes: Fix a k -simplex σ . If σ is contracted, that is, two of its boundary vertices are identified, every simplex of Γ_1 incident to $\hat{\sigma}$ is also contracted. It follows that $\gamma'_p(h_1(\sigma)) = 0 = h_2(\gamma_p(\sigma))$. On the other hand, if σ is not contracted, every simplex in the barycentric subdivision that is incident to $\hat{\sigma}$ is mapped to a non-trivial k -chain, and it is easy to verify that $\gamma'_p(h_1(\sigma)) = h_2(\gamma_p(\sigma))$ also in this case.

Summarizing the previous two steps, we have the commutative diagram

$$\begin{array}{ccc}
H_1(X_1) & \xrightarrow{i} & H_1(X_2) \\
p_1^* \uparrow & & p_2^* \uparrow \\
H_1(\Delta X_1) & \xrightarrow{\xi} & H_1(\Delta X_2) \\
q_1^* \downarrow & & q_2^* \downarrow \\
H_1(\Gamma_1) & \xrightarrow{\gamma} & H_1(\Gamma_2) \\
h_1^* \uparrow & & h_2^* \uparrow \\
H_1(\text{Nrv}\mathcal{U}^{\alpha_1}) & \xrightarrow{\gamma} & H_1(\text{Nrv}\mathcal{U}^{\alpha_2})
\end{array}$$

According to [20, Prop.4G.2 and 4G.3], the maps p_i and q_i are isomorphisms, and according to [30, Thm.13.3 and 17.2], h_i is an isomorphism. It follows that with $\theta_i^* := p_i^* \circ (q_i^*)^{-1} \circ h_i^*$, the middle square of (2) commutes, which completes the proof. \square

We apply the previous theorem on the case of restricted offset filtrations and prove Theorem 10:

Theorem 22. *For convex polygonal sites in \mathbb{R}^2 , the 0- and 1-barcode of the restricted nerve filtration are equal to the 0- and 1-barcode of the offset filtration, respectively.*

Proof. For the 1-barcode, it is enough to show that the restricted offset filtration yields a sane tisk-filtration according to Definition 20. By assumption, the restricted offsets are in generic position and interior-disjoint. It remains to show that for any α , any surrounded region is filled.

Consider a region R surrounded by A and B with boundary curves a and b . Let v_1, v_2 denote the points on the boundary of R that lie in $a \cap b$. Assume wlog that $d(v_1) \leq d(v_2) =: w$. We have to show that the union of the restricted w -offset sites cover R . For that, it suffices to show that the unrestricted w -offsets of A and B cover R , what we show next. It can easily be seen that the bisector of A and B has a segment within R that connects v_1 and v_2 . With Lemma 6, we have that $d(x) \leq w$ for all x on that bisector segment. Moreover, for any x on the part of $a \setminus b$ that bounds R , we must have $d(x) \leq w$ as well. Combining these two properties, the “half-region” of R bounded by $a \setminus b$ and the bisector segment satisfies $d(x) \leq w$ on its boundary and by convexity of the distance function, $d(x) \leq w$ in the whole region. Applying the same argument on the other half-region, we get the result.

The result for the 0-barcode is obtained by proving that an analogue version of Lemma 18 also holds for 0-homology. The proof for that is similar, but simpler than for the 1-homology case. We omit further details. \square